A COMPARISON OF COMPUTATIONAL FLOW SEPARATION PATTERNS AROUND ELLIPSOIDS WITH DIFFERENT AXES RATIOS

ICAS-94-5.7.1

Yuan Li† Hsing Tingding Zhuang Fenggan
Beijing University of Aeronautics and Astronautics, Beijing 100083, P.R.C

Abstract

The flow separation patterns around ellipsoids with different axes ratios are studied numerically in order to gain insight into the influence of body geometry. The flowfield results are steady-state solutions of the three-dimensional, incompressible Navier-Stokes equations obtained by using pseudo-compressibility method and Beam-Warming approximate factorization scheme. The separated flow patterns at 10° incidence are displayed via the computed skin-friction lines, off-surface streamlines and their Poincaré projection in the cross-flow plane. The main features are that the open separation is found only on thinner ellipsoids while the closed separation occurs on bodies with various geometries. Tornado-like vortex can be formed on the closed separation line on a fatter body. As the thickness decreases, the open separation occurs at a much more forward position and the resulted primary vortex becomes stronger. Comparison of the aerodynamic loads indicates the lift and pitching moment to increase with the decrease of thickness. An inference can be made that as long as the thickness ratio decreases toward zero, the open separation might begin in the nose and produce the strongest vortex.

Introduction

Three-dimensional flow separation and vortex motions have received much attention because of their significant effects on the aerodynamics of flight vehicles. From the following two examples we can see how important the three-dimensional flow separation and the resulted vortex might be. A stable, concentrated vortex formed by the flow separation at the leading edge of a slender wing generally contributes significant nonlinear aerodynamic loads at moderate to high angle of attack and the vortices shedding periodically from the axisymmetric bodies will cause servere side force at large incidence. Therefore, continuing efforts should be made to elucidate the effect of 3-D separation and induced vortices on aerodynamic characteristics. In the surficial topological approach, three-dimensional flow separation may be classified into two types, namely, closed and open separation[1] or global and local separation[2], but in a spatial descriptive approach, they may be further classified as closed, open and hybrid separation[3]. Different separation types are related to different physical mechanism and have different impact on aerodynamic characteristics. The closed separation results from streamwise detachment of boundary layer on the wall under streamwise pressure gradient, while the open separation exhibits the crossflow detachment of viscous shear layer from the body surface under the tangential shear between the viscous inner and inviscid outer flows. The closed separation generally produces a bubble or tornado-like vortex influencing mainly the drag of a flight vehicle, however the open separation usually produces concentrated vortex having significant effects on lift, pitching moment and also on side force in the case of asymmetric flow.

The flow separation patterns and the resulted vortex strength are related to many factors, among which the geometry is a dominant one. It is the purpose of our study to find out the relationship between the geometry and the flow separation patterns. We restrict our investigation to symmetric flow and leave asymmetric one over to future research. For clarity yet no loss of generality, we have chosen ellipsoids with different axes ratios as test cases, because flows past such bodies are able to exhibit typical separation patterns. By varying the axes ratio, the ellipsoids will resemble a large variaty of configurations from fuselage to slender wing.

Although previous studies put much emphasis on the nature of 3-D separation[4-8], yet few of them have noticed the relationship between the patterns of 3-D separation and the aerodynamic loads. A previous study[1] revealed that open separation

The project was supported by National Natural Science Foundation of China under contract No. 9188010.

† Present address: Institute of mechanics, Chinese Academy of Sciences, Beijing 100080.

becomes dominant as a prolate spheroid becomes more slender. In order to gain further insight into the influence of geometry with the hope of finding the relationship between the evolution of separation patterns and the axes ratio, we present a comparative study of the flowfield around ellipsoids with five different axes ratios. The axes ratios of a:b:c for the five cases are 1:0.25:0.25 (labelled as case A), 1:0.25:0.167 (B), 1:0.25:0.1 (C), 1:0.5:0.25 (D) and 1:0.5:0.167 (E), where a, b and c refer to half axis length in streamwise, spanwise and normal directions respectively, see Fig.1. So we can find out the influence of the thickness ratio (c/a) by comparing among A,B,C or between D and E cases, and the influence of slenderness ratio (b/a) by comparing A with D, or B with E. The flowfields are numerical solutions to incompressible Navier-Stokes equations. For solving the equations, the pseudo-compressibility method is used because of its validity and efficiency in computing steady 3-D incompressible flow[9,10]. The addition of an artificial time derivative of pressure to the continuity equation will render the incompressible equations hyperbolic. Beam-Warming approximate factorization scheme is applied. Our algorithm is similar to that of Kwak et al [9] but different in artificial viscosity coefficient and adoption of local time step to accelerate the convergence to steady-state. Surface skin-friction lines, streaklines issued from points nearest to the wall and their poicaré cut in the crossflow plane are used to define the pattern of 3-D separation. Based on these charts the flow separation patterns around different geometries are revealed and a direct comparison is made. In accordance with the variation of the flowfield, the aerodynamic characteristics are also discussed.

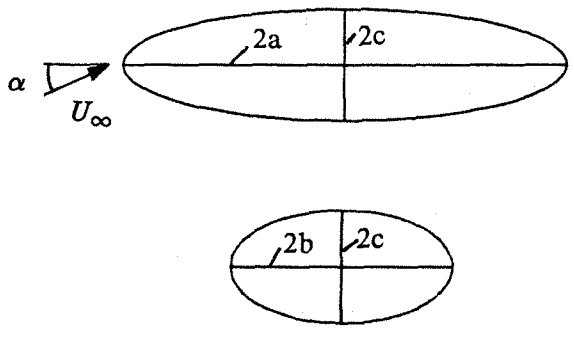

Figure 1. Sketch of the ellipsoid

Governing equations and numerical algorithm

The flow computation is governed by incompressible Navier-Stokes equations. To implement a time marching scheme, a pseudo-compressibility term is added to the continuity equation as follows

$$\frac{1}{\beta}\frac{\partial p}{\partial \tau} + \nabla \cdot \vec{u} = 0 \tag{1}$$

where β is a constant called pseudocompressibility factor and τ is the time.

In body-fitted curvilinear co-ordinate system, the governing equations can be formulated as

$$\frac{\partial Q}{\partial \tau} + \frac{\partial (E - E_\nu)}{\partial \xi} + \frac{\partial (F - F_\nu)}{\partial \eta} + \frac{\partial (G - G_\nu)}{\partial \varsigma} = 0 \tag{2}$$

where ξ, η and ς are coordinates along streamwise, circumferential and normal direction respectively. The formulations for conservative variable vector Q, inviscid flux terms E, F, G and viscous terms E_ν, F_ν, G_ν can be found in Ref.[9]. A nondimensional form of the equations is used througthout the computation. Lengths are scaled by the longitudinal axis length L, velocity components by the free-stream velocity U_∞ and dynamic pressure by ρU_∞^2.

The numerical algorithm used to solve Eq.(2) is an implicit, approximately factorized, finite-difference scheme(AF scheme) by Beam and Warming. By using backward difference for time and central difference for inviscid and viscous terms, AF scheme with 2nd order implicit and 4th order explicit artificial dissipation added in the left-hand side and right-hand-side respectively can be expressed as

$$L_\xi L_\eta L_\varsigma \triangle D^n = RHS^n \tag{3}$$

where

$$L_\xi = I + h\delta_\xi \hat{A} - h\bar{\delta}_\xi \left[\frac{R_e^{-1}}{J}(\nabla\xi \cdot \nabla\xi) I_m \delta_\xi\right] - \Delta\tau\epsilon_2 \delta_\xi^- \delta_\xi^+$$

$$L_\eta = I + h\delta_\eta \hat{B} - h\bar{\delta}_\eta \left[\frac{R_e^{-1}}{J}(\nabla\eta \cdot \nabla\eta) I_m \delta_\eta\right] - \Delta\tau\epsilon_2 \delta_\eta^- \delta_\eta^+$$

$$L_\varsigma = I + h\delta_\varsigma \hat{C} - h\bar{\delta}_\varsigma \left[\frac{R_e^{-1}}{J}(\nabla\varsigma \cdot \nabla\varsigma) I_m \delta_\varsigma\right]$$

$$-\Delta\tau\epsilon_2\delta_\varsigma^-\delta_\varsigma^+$$

$$RHS^n = -h\Big[(\delta_\xi E + \delta_\eta F + \delta_\varsigma G) -$$

$$(\bar{\delta}_\xi E_\nu + \bar{\delta}_\eta F_\nu + \bar{\delta}_\varsigma G_\nu)\Big] -$$

$$\Delta\tau\epsilon_4\Big[(\delta_\xi^-\delta_\xi^+)^2 + (\delta_\eta^-\delta_\eta^+)^2 + (\delta_\varsigma^-\delta_\varsigma^+)^2\Big]D^n$$

$$\Delta D^n = D^{n+1} - D^n$$

with $h = \Delta\tau J$ and $D = Q/J$. δ_ξ is a typical three-point, second-order-accurate, central difference operator. $\bar{\delta}_\xi$ is a midpoint operator used in viscous terms, δ_ξ^+ and δ_ξ^- are forward and backward difference operators respectively. J denotes the Jacobian of the coordinate transformation. I is an identity matrix and I_m is a diagonal matrix with 0 for the first element and 1 for the others. Only orthogonal viscous terms are retained in left-hand-side factors. The analytical expressions of the inviscid flux Jacobian matrices $\hat{A}, \hat{B}$ and $\hat{C}$ are also included in ref.[9].

The above scheme is formally second-order accurate and conditionally stable usually under the condition of $\epsilon_2 \geq 2.0\epsilon_4$ and $\epsilon_4 = O(1)$, ϵ_2 and ϵ_4 are artificial viscosity. Note that all artificial dissipation terms are multiplied by time step $\Delta\tau$, which is different from Kwak's. This treatment provides appropriate dissipation in the boundary layer when local time step is used. In present study, We took $\epsilon_2 = 3\epsilon_4$ and $\epsilon_4 = 0.5 \sim 1.0$, which were large enough to maintain numerical stability and reasonable in having little effect on quantities of skin-friction especially without changing the qualitative features of the flow patterns. To speed up the convergence toward steady-state, local time step was adopted based on a Courant number of 5. However an upper limit of time step has to be imposed to prevent the computation from instability and inaccuracy.

The constant β determines how "compressible" the modified velocity field is, and has influence on stability, convergence rate, and accuracy of the numerical solution. Previous numerical study[11] as well as our experience shows that $\beta = 1$ is a preferable choice for steady-state computation.

In order to achieve higher computational efficiency, the scheme(3) can be diagonalized[12] as long as the matrix I_m in viscous terms is changed into an identity matrix I. Diagonalization can reduce CPU time by nearly 50%.

Initial and boundary conditions

The initial condition is that of uniform freestream flow everywhere except $u = v = w = 0$ on the body surface. The boundary conditions are treated explicitly. On the surface the non-slip condition is applied, i.e.

$$u = v = w = 0 \tag{4}$$

and the pressure computed via a normal momentum equation taken on the wall from Eq.(2), e.g.

$$\frac{\partial p}{\partial n} = R_e^{-1}\frac{\partial^2 v}{\partial n^2} \tag{5}$$

with n and v normal to the surface. The treatment of the condition in the farfield is based on characteristics analysis normal to the farfield boundary via

$$\frac{\partial W}{\partial \tau} + \Lambda_n\frac{\partial W}{\partial n} = 0 \tag{6}$$

where $\Lambda = diag(q_n, q_n, q_n + a, q_n - a)$,
$a = (q_n^2 + \beta)^{1/2}$ and W is the characterictics variable vector. In our steady-state computation, for outflow boundary with $q_n \geq 0$, W_1, W_2, W_3 are determined from inner flow variables and W_4 from external freestream flow. For inflow boundary with $q_n \leq 0$, W_1, W_2, W_4 are determined from external freestream flow and W_3 from inner flow variables. Once W is known, the flow variable can be obtained.

Reflection conditions are used on the windward and leeward symmetry planes. On the major axis extending from the nose and the tail, all variables are equal to the average of values at the same normal position but next ξ = constant plane.

Results and discussions

The results herewith included are obtained from the laminar flow computation for an incidence $\alpha = 10°$ and a Reynolds number Re_L=11700. The five cases with a:b:c equal to 1:0.25:0.25, 1:0.25:0.167, 1:0.25:0.1, 1:0.5:0.25 and 1:0.5:0.167 are labelled as A, B, C, D and E. We define c/a as thickness ratio and b/a slenderness ratio.

The outer boundary of the solution domain extends 1.25 times the length of the major axis from the body in upstream and downstream directions. Doubling this distance does not change the results appreciably. The grids are of O-O type generated by a transfinite interpolation method[13]. Typical grid number is 37 × 33 × 49. To define a steady state, the residual of Eq.(3) and divergence of velocity would converge by four and three orders-of-magnitude respectively. Generally this will require

about 2000-3000 iterations. We will focus on discussions of the relations between the geometry and the flow characteristics.

Topological changes of surface flow patterns with axes ratios

In Figure 2, the computed skin-friction lines and the corresponding topological structures for the five cases are shown. For case A, corresponding to the flow past a prolate spheroid, the line $S_1 - F_1 - S_2 - F_2 - S_3$ is a closed separation line which divides the skin-friction lines coming from the front and rear stagnation points. Here two foci F_1 and F_2 on this line are often associated with tornado-like vortices. The skin-friction lines originating from the front stagnation point approach the rear and show the tendency of slight squeezing in front of the closed separation line but rather difficult to discern the existence of open separation. For case B and C open separation line is formed evidently at further forward position and approaches toward the windward side symmetry plane. We see the topological changes from case B to C resulting from the disappearance of focus F_1 and F_2. The comparison of case D with E also shows an earlier and much evident open separation which occurs on ellipsoid with smaller thickness ratio. For comparing the influence of slenderness ratio we compare case A with D, or B with E. We see the larger slenderness ratio results in a much forward extension of the whole separated region including the sad-

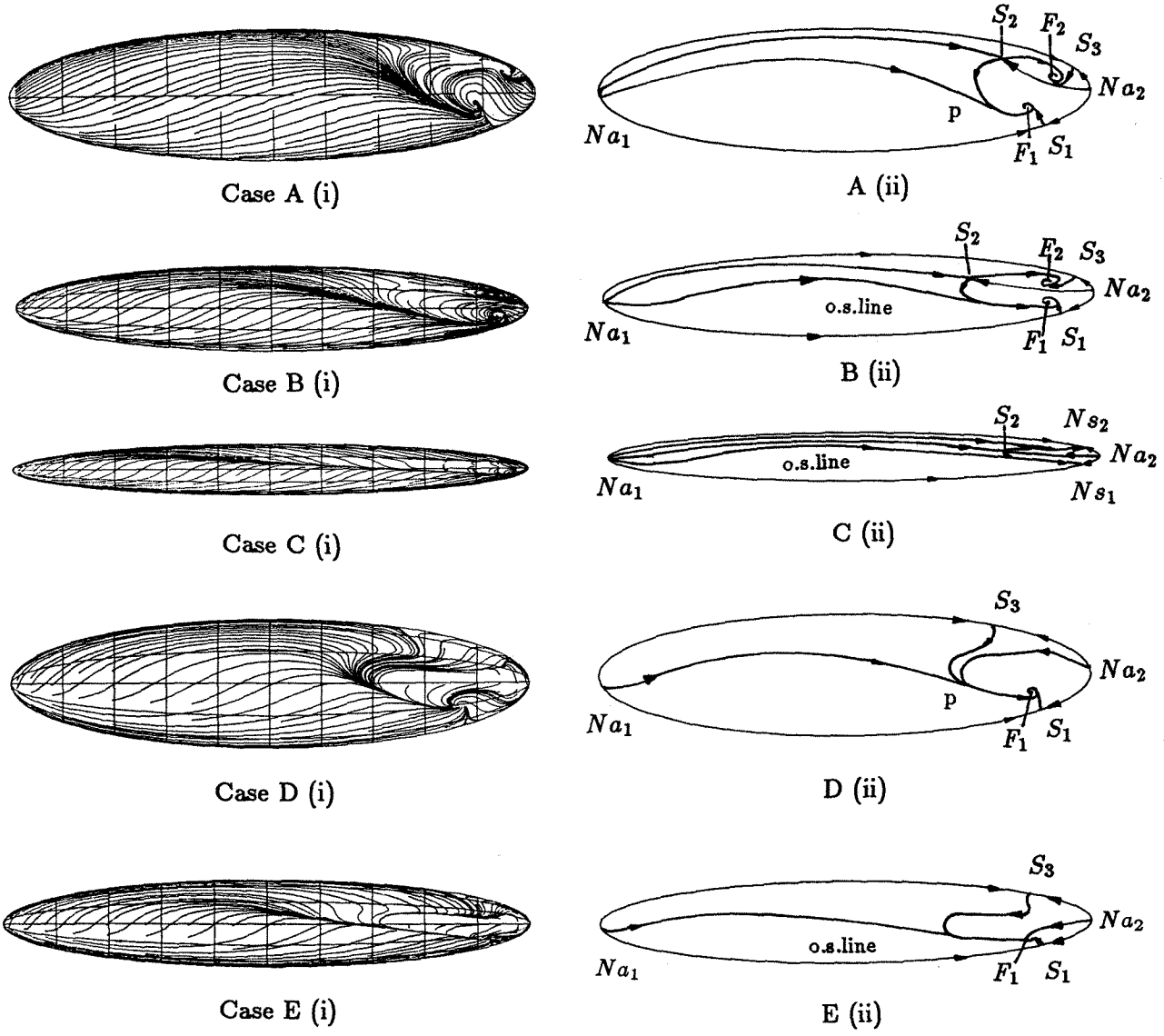

Figure 2. Comparison of the skin-friction line patterns(i) and their topology(ii) at $\alpha = 10°$, $Re_L = 11700$.

dle point S_3 on the leeward side symmetry plane. However the open separation in case D differs a little from case A with smaller slenderness ratio. The common feature of case D and E is the disappearance of S_2 and F_2 and the bubble region after the leeward segment of the the closed separation line $S_1 - F_1 - S_3$ is very large. From the comparsion described above, we see the normal and lateral scales of a body would influence the open and closed separation respectively. Making the body thinner will significantly promote the happening of open separation while increasing the slenderness ratio would extend a closed separation region. The physical reason why decreasing the thickness ratio can promote open separation may be understood from the variation of pressure gradient in the crossflow plane. In Fig.3 where pressure gradients along the circumferential direction of the body surface are compared between case D and E, we see a larger gradient is developed for smaller thickness ratio case E, which indicates the cause that the open separation is more likely to occur on thinner ellipsoid.

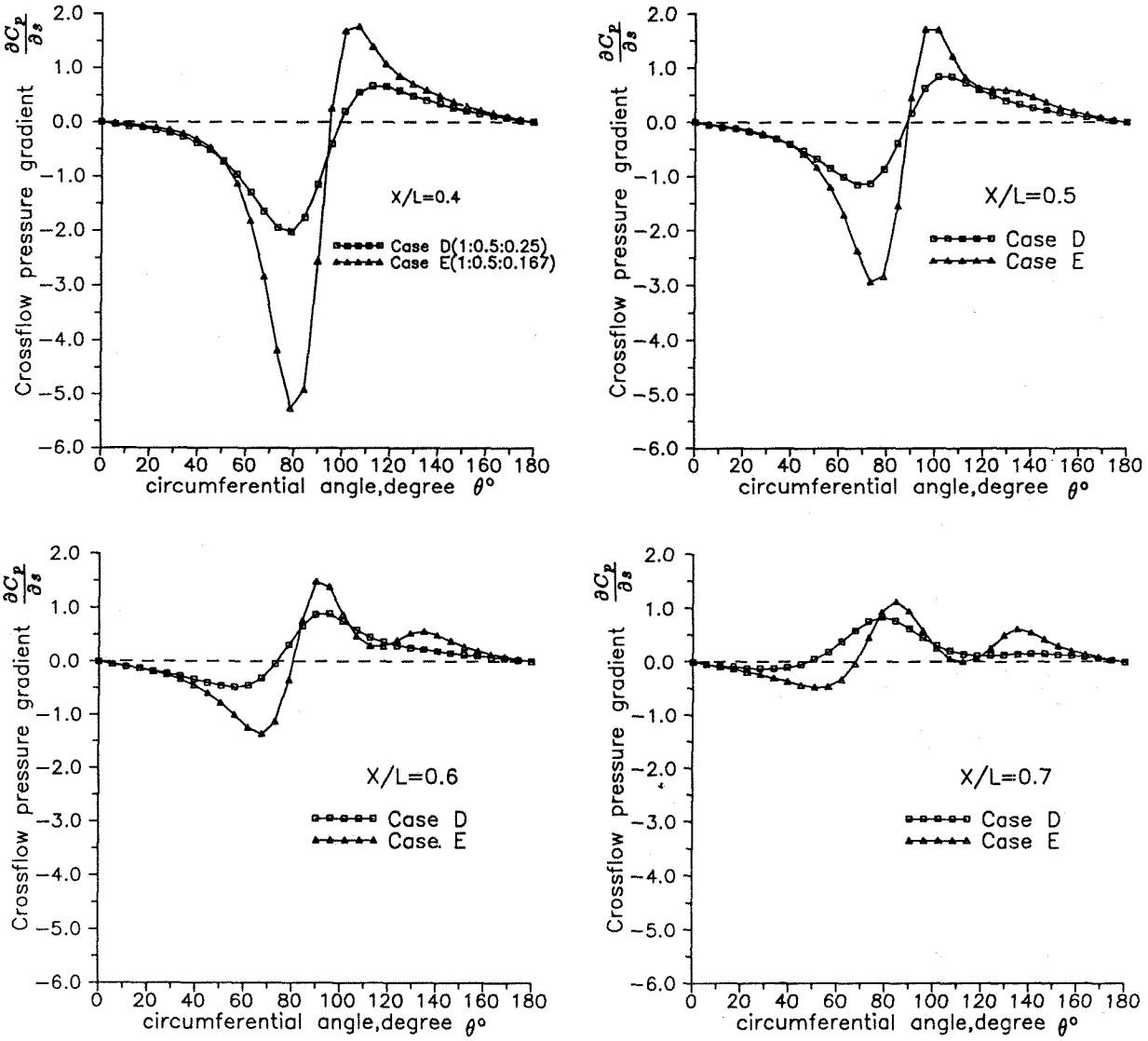

Figure 3. Comparison of the surface pressure gradient along the circumferential direction between case D ($\frac{c}{a} = 0.25$) and E($\frac{c}{a} = 0.167$) at four axial stations.(θ=0 at the windward symmetry)

Spatial and cross-sectional flow patterns

It seems insufficient to determine the 3-D separation type only from the skin-friction line patterns. However, the separation pattern might well be delineated from the 3-D streamlines and the flow features in some appropriate cross-sections.

Figure 4 shows the off-surface streamlines in the five cases. The streamlines issued from the grid points nearest to the body surface will usually detach themself from the body surface along the saddle–node (including focus) segment of the closed separation line or near a converged open separation line. In our computation, there are tornado-like vortices at two foci F_1 and F_2 in case A and B, but by the decreasing thickness ratio they will disappear as shown in case C. As the slenderness ratio increases(from case A to D or from B to E), the vortex at leeward focus F_2 disappears and the one at focus F_1 becomes weaker. The influence of thickness ratio on open separation is evidently illustrated in the sequence A→B → C or D → E. For example, open separation in case B occurs at $\frac{X}{L} \approx 0.65$ and tends to roll up after $\frac{X}{L} \approx 1.0$. In case C, open separation happens as early as at $\frac{X}{L} \approx 0.45$ and the separated shear layer begins to roll up to form primary vortex at $\frac{X}{L} \approx 0.75$. In order to describe the separation more clearly, the so-called Poincré cut is given. It is the projection of intersection of the streaklines released from all points nearest to the body surface onto a plane normal to the major axis . In Figure 5 the Poincré cuts show the viscous shear layer from the open separation in case C rolls more tightly than in case B at the same axial station. Figure 6 shows the comparison of axial vorticity distribution for case B and C at several axial stations. We see an earlier formation of a vortical region in case C, and the vorticity in outer vortical region in case C is greater than in case B at $\frac{X}{L}$=0.95. This indicates the vortex strength in case C is greater than in case B. This comparison shows that the primary vortex due to open separation occurs earlier and becomes stronger as the thickness ratio decreases.

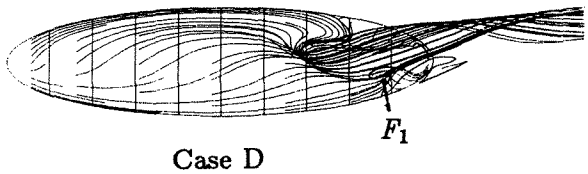

Case D

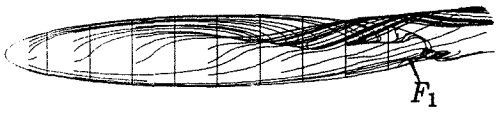

Case E

Figure 4. Off-surface streamlines illustrating the separation patterns on ellpsoids with different axes ratios.

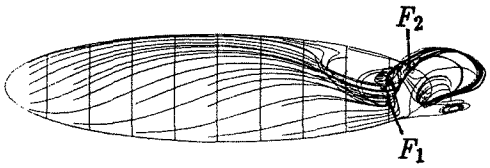

Case A

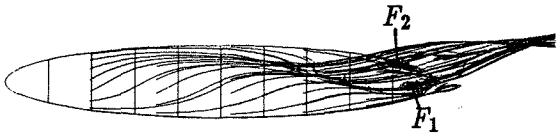

Case B

Case C

Aerodynamic loads

To see how aerodynamic loads are related to flow separation patterns, the lift, drag and pitching moment are computed from the surface pressure and wall shear stress. Denoting by C_L, C_D and C_M respectively, the coeffcients of lift, drag and pitching moment are defined as

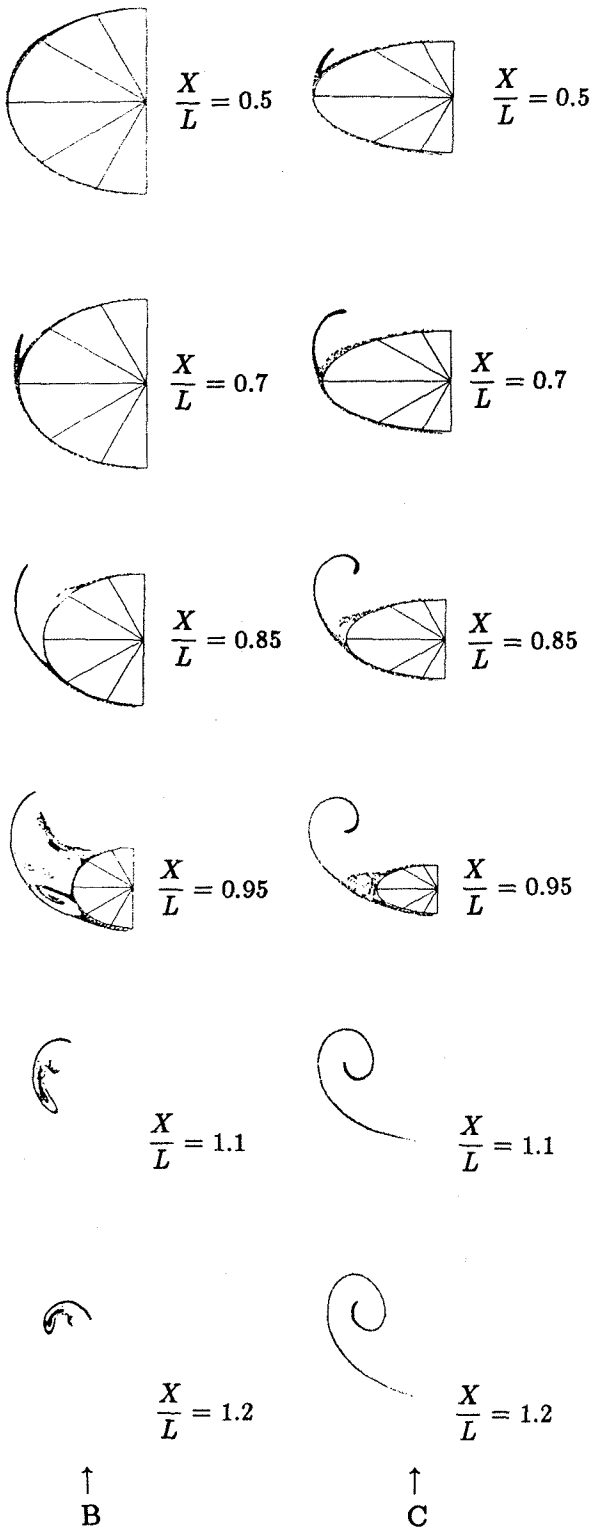

Figure 5. Comparison of Poincaré cuts of the viscous shear layer emanating from near the body surface between case B($\frac{c}{a} = 0.167$) and C($\frac{c}{a} = 0.1$).

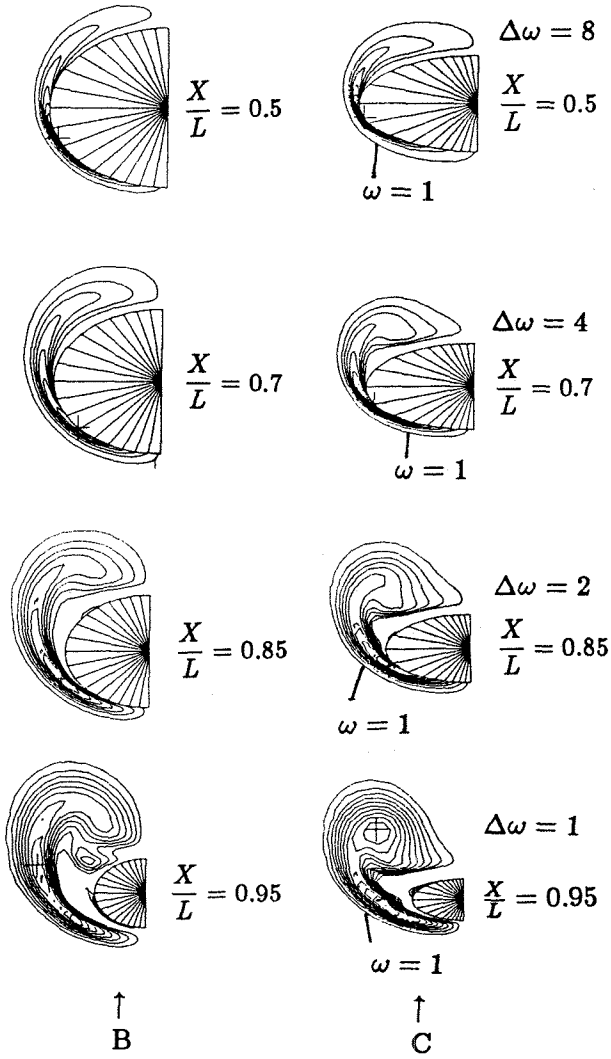

Figure 6. Comparison of the axial vorticity ω distribution between case B and C. + denotes where maximum vorticity exists. $\Delta\omega$ is the increment of vorticity between two adjacent lines.

$$C_L = \frac{2}{\rho U_\infty^2 S} \int\int (\tau_w - p\vec{n}) \cdot \vec{e}_\perp dS$$
$$C_D = \frac{2}{\rho U_\infty^2 S} \int\int (\tau_w - p\vec{n}) \cdot \vec{e}_\infty dS \qquad (7)$$
$$C_M = \frac{2}{\rho U_\infty^2 S L} \int\int \vec{r} \times (\tau_w - p\vec{n}) dS$$

where $\vec{\tau}_w$ is surface stress vector , $\vec{e}_\infty$, $\vec{e}_\perp$ and $\vec{n}$ are unit vector along and normal to the free stream direction, and normal to the body surface respectively. S is the projection area from the top and $\vec{r}$

denotes the position vector from the center of the major axis to the element dS. Fig.7 shows the variation of aerodynamic loads with thickness ratio at 10° incidence. The C_L and C_M increase with the decrease of thickness ratio, which is consistent with the fact that the primary vortex due to open separation provides nonlinear aerodynamic loads because the flow past thinner ellipsoid produces stronger primary vortex and larger area dominated by the open separation. Comparing Fig.7 (c) to (e), we see C_{Dp} is larger but C_{Df} is smaller for larger slenderness bodies(D and E). However, the total drag is nearly the same for different slenderness bodies.

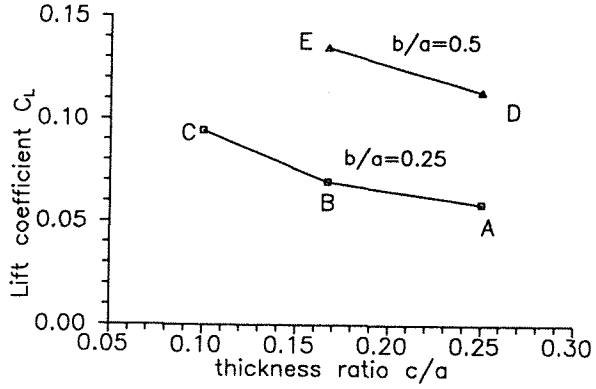

(a)

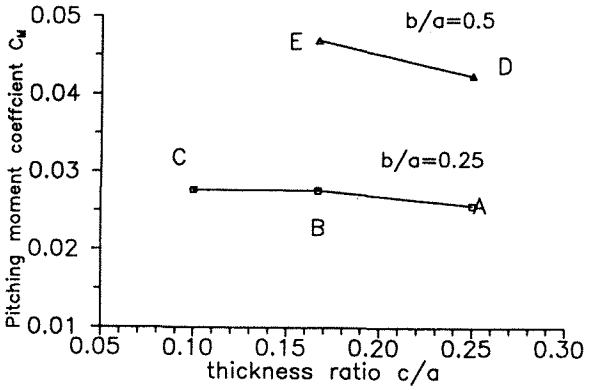

(b)

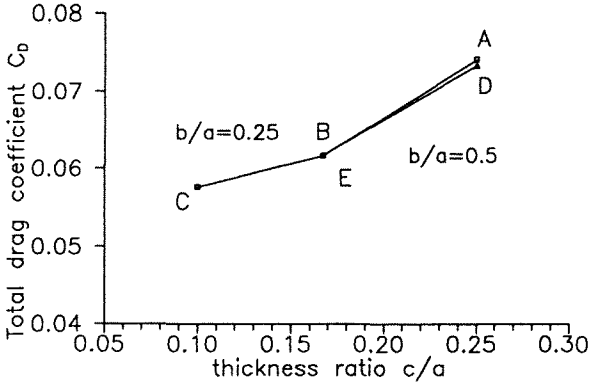

(c)

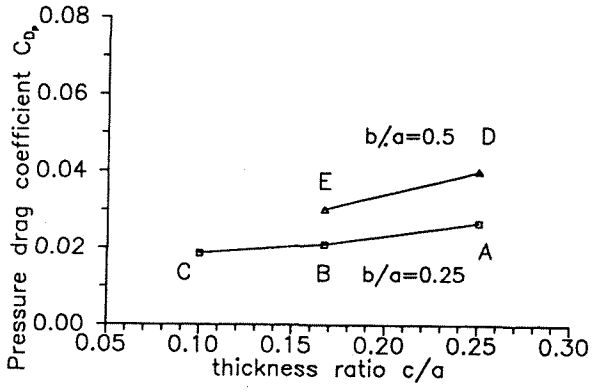

(d)

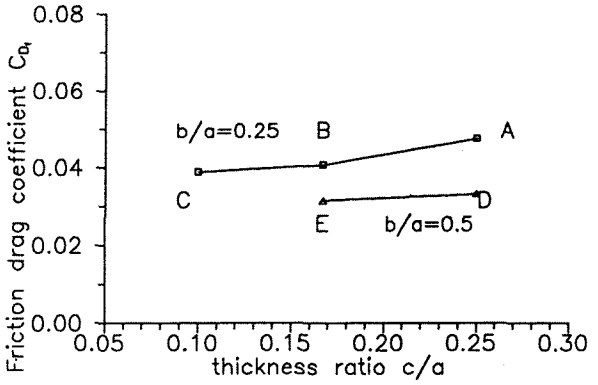

(e)

Figure 7. Variation of the coefficients of Lift C_L, pitching moment C_M and drag C_D with the thickness ratio. $\alpha = 10°, Re_L = 11700$.

Conclusions

The incompressible flows over ellipsoids with five axes ratios have been studied by solving the 3-D incompressible complete Navier-Stokes equations numerically. The separated flow patterns are compared with respect to different axes ratios. Flow patterns are determined via the computed skin-friction lines, off-surface streamlines and their Poincaré cuts in appropriate crossflow planes. Common feature can be deduced that there is always a region of closed separation at the rear part of the body identified by the skin-friction line having critical points. Tornado-like vortex may exist on this line and become evident as the ellipsoid becomes thicker. The evidence of open separation is illustrated by the squeeze of skin-friction lines in the region where skin-friction vector field has no critical point, the detachment of off-surface

streamlines and the trend of rolling up viewed in a Poicaré plane. The open separation will occur earlier if thickness ratio decreases, and the area behind the closed separation line will expand if the lateral scale increases. The primary vortex formed by the rolling-up of open separated shear layer will become stronger for thinner ellipspoids. These change of flow patterns with body geometry affects the aerodynamic loads in a consistent way with the well-known fact that the open separation-induced vortex usually produces large nonlinear aerodynamic loads through the change of pressure. Finally an inference can be made that open separation might begin in the region at the apex and form the strongest separated vortex when the thickness approaches zero.

References

1. Wang, K. C., Zhou, H.C., Hu, C.H. and Harrington, S., Three- Dimensional Separated Flow Structure over Prolate Spheroids , Proc. R. Soc. London, Vol. A421, (1990):73-90.
2. Yates, L.A. and Chapman, G.T., Streamlines, Vorticity Lines, and Vorticies around Three-Dimensional Bodies, AIAA J. Vol.30, No.7, (1988):1819-1826.
3. Zhang, H.X., Shen, Q. and Gao, S.C., Numerical Simulation and Analysis for Hypersonic Flow with Separation over Blunt Cone at Angle of Attack, *Acta Arodynamica Sinica*, Vol.9, No.2, (1991):160-174.
4. Eichelbrenner, E. A., Qudart, A., La Recherche Aeronautique, n 47, (1955): 11-14.
5. Costis, C.E., Hoang, N.T. and Telionis, D,.T., Laminar Separating Flow over a Prolate Spheroid, J. Aircraft, Vol.26, (1989):810-876.
6. Su, W.H., Tao Bo and Xu Li, Experimental Investigation of Three-Dimensional Separated Flow over a Prolate Spheroid, Int. Conf. Experimental Fluid Mechanics, Chengdu, China, 1991.
7. Vatsa, V.N, Thomas, J.L. and Wedan, B.W., Navier-Stokes Computations of a Prolate Spheroid at Angle of Attack, J. Aircraft, Vol.26, (1989):986-993.
8. Kim, S.E. and Patel, V,C., Laminar Separation on a Spheroid at Incidence, AIAA P 91-1803, 1991.
9. Kwak, D., Chang, J.L.C., Shanks, S.P. and Chakravarthy, S.R. ,An Incompressible Navier-Stokes Flow Solver in Three-Dimensional Curvilinear Coordinate Systems Using Primitive Variables, AIAA P 84-0253, 1984.
10. Rogers, S.E., Kwak, D. and Kaul, U., On the Accuracy of the Pseudocompressibility Method in Solving the Incompressible Navier-Stokes Equations, AIAA P 85-1689, 1985.
11. Hsu, C.H., Hartwich, P.M. and Liu, C.H., Incompressible Navier-Stokes Computations of Vortical Flows over Double -Delta Wings, AIAA P 87-1341, 1987.
12. Rogers, S.E., Chang, J.L.C. and Kwak, D., A Diagonal Algorithm for the Method of Pseudocompressibility, J. Compt. Phys., Vol.73, (1987):364-379.
13. Eriksson, L.E., Generation of Boundary-Comforming Grids around Wing-Body Configurations Using Transfinite Interpolation. AIAA J. Vol.20, No.10, (1982):1313-1320.